Journal

ACS Nano

ISSN

1936-0851

Authors

Kim, Woojo

Xia, Zihan

Zhao, Tianyu

et al.

Publication Date

2026-07-21

DOI

10.1021/acsnano.6c00638

ACS NANO

www.acsnano.org

Retinomorphic Organic Infrared Imager Selectable between Frame-Based and Event-Driven Detection Modes

Woojo Kim, Zihan Xia, Tianyu Zhao, Sanyukta Datta Gupta, Soong Ju Oh, Jason D. Azoulay, Mingu Kang,* and Tse Nga Ng*

Cite This: https://doi.org/10.1021/acsnano.6c00638

Read Online

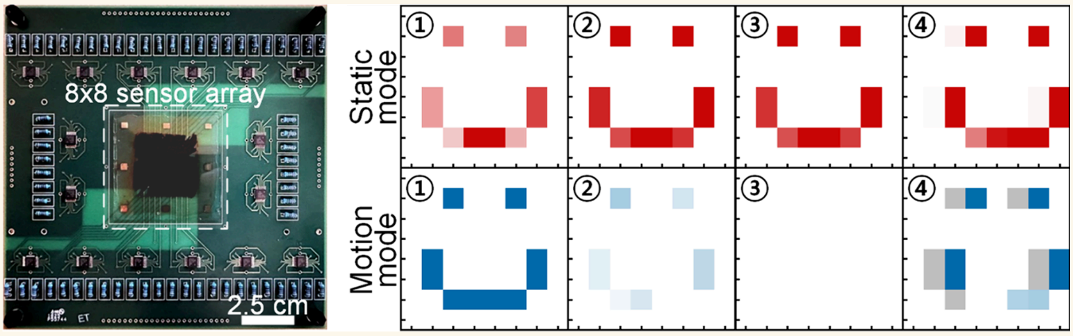

ABSTRACT: This study presents a reconfigurable retinomorphic infrared imager that can be electrically switched between two complementary modes: a motion mode that delivers streamlined spiking outputs for efficient motion tracking and a static mode that integrates charge to capture high-fidelity images. Mode selection is achieved at the device level by tuning the variable resistance in a photocapacitor−transistor architecture. This work also establishes measurement guidelines for time-derivative sensors to evaluate rate-dependent detection limits. To demonstrate scalability and integration capability, 8 × 8 pixel arrays are fabricated and integrated with silicon integrated circuits, enabling spatiotemporal imaging in dual modes. This device-level approach reduces circuit overhead traditionally required for multimodal operation and offers a compact configuration for lowering energy consumption and facilitating high-density integration in next-generation vision systems.

KEYWORDS: *retinomorphic photodetector, organic semiconductor, photocapacitor, time-derivative sensor, motion tracking*

Conventional imaging systems capture data at fixed frame rates that often result in redundant information, contributing to unnecessary power use and processing delays. To address these shortcomings, event-driven pixel circuits incorporate in-sensor computing elements to locally streamline signals, though prior silicon implementations remain constrained by circuit complexity and large footprint.[1−4] Instead of relying solely on traditional circuit-level signal processing, device-level innovations have emerged to emulate processing functions through inherent physical mechanisms,[5−9] such as leveraging charge trapping for intensity adaptation[10−12] and memristive hysteresis for spike encoding[13−15] functions inspired by biological retina. The retinomorphic devices replace large circuits with compact designs that lower the energy consumption and facilitate high-density integration.

A class of retinomorphic photodetectors using a photo-capacitor-resistor design has recently been developed for efficient motion detection,[16−22] where spike pulses are generated in response to dynamic changes but not under static illumination, thus providing a built-in feature-extraction mechanism that is particularly suited to hone in on moving objects and pruning unchanged background. However, discarding all static data will limit image reconstruction and fidelity, and many applications will benefit from the flexibility to switch on demand between event-driven motion detection and high-fidelity framed-based imaging.[23,24] This work tackles the

Received: January 12, 2026
Revised: June 11, 2026
Accepted: June 12, 2026

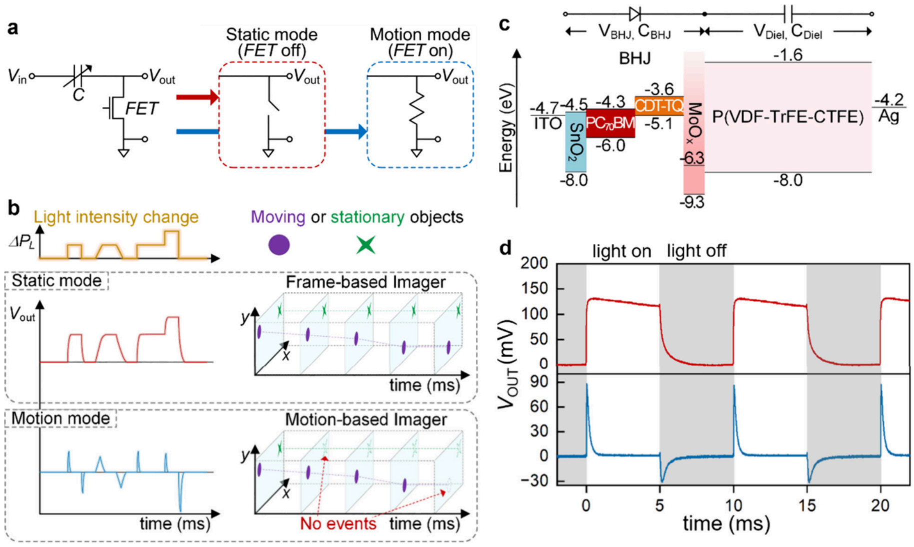

Figure 1. Reconfigurable design to operate in frame-based static or event-driven motion mode. (a) Sensor circuit consisting of a photocapacitor and a field-effect transistor. Controlling the FET gate bias adjusts the channel resistance and switches the pixel operation between static and motion modes. Illustrations comparing (b) the sensor signals and image generations in static and motion modes. (c) Energy band diagram of materials in the photocapacitor. (d) V_{out} of the photosensor under 980 nm light modulation of 1.1 mW/cm^2 when the FET is off (V_{GS} = 0 V and V_{DS} = 1.8 V, red trace) and when FET is on (V_{GS} and V_{DS} = 1.8 V) and connected to a 100 kΩ resistor (blue trace).

reconfiguration challenge by device-level modifications, offering a straightforward path to dual-mode operation not achieved in conventional circuits. In the retinomorphic design here, the discharge bandwidth is made tunable by adjusting the resistance with transistor control, allowing the photodetector either to deliver spiking output for rapid motion tracking or to integrate signal over a frame period for conventional imaging, selectable by simple electrical biasing.

In examining device operation in event-driven mode, this work systematically evaluates the spiking amplitude and timing as functions of motion speed and background lighting. As a transient sensor, the device performance depends on the rate of illumination change ($\Delta P/t$), but prior studies primarily reported responses to illumination change (ΔP) while overlooking the temporal rate ($1/t$) aspect. By clarifying the rate dependence, the analysis here improves the characterization of device responses to transient stimuli and underscores measurement guidelines that are broadly applicable to time-derivative sensors capturing changes in the environment.

In addition, integration of sensors with silicon readout circuits remains a major challenge. The large difference in dimensions between nanometer-thick sensors and micrometer-thick silicon chips or printed circuit board structures leads to a significant mismatch in interfacial roughness. Such a mismatch creates voids and nonuniform contact areas, resulting in electrical discontinuities, increased leakage currents, and local mechanical or thermal stress concentrations. To address these integration issues, this work also demonstrates a bonding process onto PCB toward the goal of enabling co-design and heterogeneous integration between sensors and processors.[25−33]

The reconfigurable retinomorphic devices are integrated into 8 × 8 pixel arrays to demonstrate scalability and contrast the imaging performance of the two operational modes. The sensor materials based on organic infrared semiconductors[34−37] allow low-temperature processing and large-area coverage, with a spectral range from 600 to 1300 nm. The patterned sensor arrays are bonded onto printed circuit boards (PCB) mounted with silicon integrated circuits (ICs) for readout control. The process flow for sensor-PCB bonding overcomes interfacial mismatch challenges in heterogeneous integration and enables rapid testing with different IC designs before direct on-chip integration, leading to proof-of-concept results paving the path toward efficient multimodal machine vision systems.

■ RESULTS AND DISCUSSION

Photodetector Design Switchable between Static and Motion Detection Modes

The original retinomorphic sensor design[16−18] used a photosensitive capacitor connected in series with a fixed-value resistor, together forming a resistor−capacitor (RC) node that functions solely as a high-pass filter. In this work, the reconfigurable design replaced the fixed resistor with a field-effect transistor (FET), enabling gate-voltage control to select between frame-based "static" and event-driven "motion" detection modes. As a side note, this FET role is different from its typical function in conventional active-matrix array, where the FET is used to select pixel addressing and not for RC control as done here. The circuit diagram in Figure 1a and the signal diagram in Figure 1b illustrate the switching concept that leverages the FET's variable channel resistance. When the gate voltage turns off the FET, the high channel resistance impedes the discharge path and appears as an open circuit; the photogenerated charges are accumulated and integrated over the frame period, same as in conventional frame-based readout. Conversely, when the FET is turned on, the low channel resistance provides a discharge path to ground, reverting to the high-pass RC filter function that allows photogenerated charges to dissipate. Under this configuration, the spiking signals come from displacement current that arises only with changes in light intensity, thereby emphasizing movement events and removing constant redundant background in the motion mode.

Within the retinomorphic sensor, the light-sensing component was the photocapacitor constructed in a metal−insulator−semiconductor capacitor design as shown in Figure 1c. The photoactive materials were organic semiconductors in a bulk heterojunction (BHJ) blend, with a 1:2 ratio of polymer donor to fullerene-derivative acceptor. The BHJ layer was responsive to light in the shortwave infrared range of 600—1300 nm,[38−40] and the materials chemical structures and absorption spectra are presented in supplemental Figure S1. The BHJ was sandwiched between electron- and hole-transporting layers of tin oxide SnO_2 and molybdenum oxide MoO_x, respectively, analogous to standard photodiode structures. The key modification in the photocapacitor structure was the addition of a dielectric layer next to the photodiode stack. Due to the insulating dielectric suppressing leakage current, this direct integration[16] reduced dark current noise, increased response speed, and enhanced signal-to-noise ratio than externally connecting individual diode and capacitor components as shown in supplemental Figure S2.

For circuit modeling, the photocapacitor was represented by BHJ and dielectric capacitances in series, C_{BHJ} and C_{Diel}, respectively, behaving as a capacitive voltage divider. The voltage drop across the BHJ layer V_{BHJ}, compared to the total voltage across the stack V_{in}, was dictated by $V_{BHJ}/V_{in} = C_{Diel}/(C_{Diel} + C_{BHJ})$. To increase the photogenerated signal, the V_{BHJ}/V_{in} ratio should be maximized, which can be achieved by designing the device with a low C_{BHJ} and a high C_{Diel}, as calculated in supplemental Figure S1e. However, lowering C_{BHJ} by increasing the BHJ thickness is practically constrained, because thicker films would hinder charge extraction with undesirable recombination. Therefore, this work chose to increase C_{Diel} by replacing Teflon dielectric (relative permittivity $\kappa \sim 2.0$) with a high-κ relaxor ferroelectric polymer (poly(vinylidene fluoride-trifluoroethylene-chlorotrifluoroethylene) terpolymer, $\kappa \sim 30$); additional details on the device materials, fabrication procedures, and characterization are provided in the Methods section and Supporting Information.

Following the fabrication and integration of the photocapacitor-FET retinomorphic sensor, Figure 1d compares its photoresponse measured under static or motion modes. In the static mode with the FET switched off, the device maintained a continuous output voltage, V_{out}, under constant illumination from a 980 nm LED. Whereas in the motion mode with the FET on, the sensor generated voltage spikes as the photocapacitor charged/discharged with illumination changes, but it returned to equilibrium and output zero volts under constant lighting.[16,21,22] The displacement current flow during charging and discharging produced positive and negative spikes (a step-by-step explanation is provided in supplemental Figure S3), whose magnitude and timing depended on the rate of illumination change, as analyzed in the following section. This feature-extraction mechanism delivers sparse streamlined data only when changes are detected, minimizing redundant data of stationary objects, as illustrated in Figure 1b, where the image of nonmoving objects fades while the data highlight dynamic features. Dual-mode imaging is presented later with results taken from integrated pixel arrays, but first we characterized the dynamic response of an individual sensor in motion mode to understand its performance limits and sensitivity to background light.

Characterization of Motion Sensor Response under Varying Stimulus Rates and Background Lighting Conditions

The output of conventional photodiodes[41] is proportional to the incident light power P_L, or equivalently to the light intensity which is power per unit area. However, for the retinomorphic photodetector here, or generally for any time-derivative sensor, the response depended on more than the absolute P_L input and rather required considering the rate of change in the input ($\Delta P/t$), where $\Delta P = P_L - P_B$, with P_B being the background illumination power, and t is the time period it takes for the illumination to change by ΔP. Accordingly, the following measurement procedures were designed to evaluate the effects of $\Delta P/t$ by varying one parameter while holding the other constant.

Vary t While ΔP Is Fixed. A fast-moving object causes a sharp change in light level, whereas a slow-moving object results in a more gradual transition. To reflect this speed change, the incident light was turned on/off at different rates to adjust the steepness of the rising and falling edges as shown in Figure 2a,b.

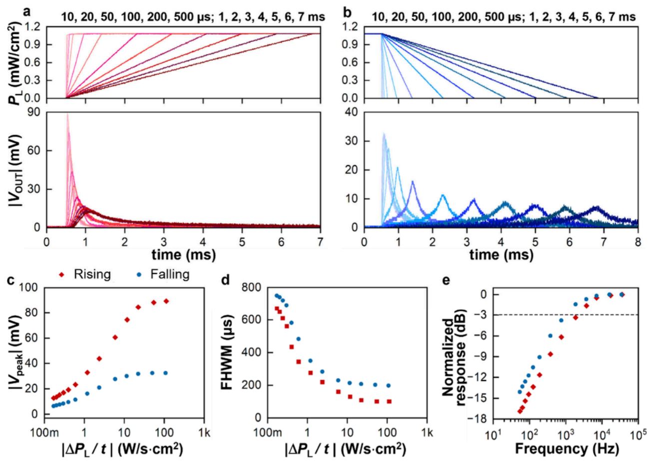

Figure 2. Sensor temporal characteristics. Measurements with a 100 kΩ resistor, under a 980 nm LED being switched on (red) and off (blue) at different speeds. Incident light intensity and corresponding sensor output versus time for various (a) rising and (b) falling periods (10 μs, 20 μs, 50 μs, 100 μs, 200 μs, 500 μs, and 1 ms to 7 ms in increments of 1 ms). (c) Sensor output voltages and (d) span at full-width half-maximum versus the rate of change in incident light power. (e) Normalized sensor signal versus transition frequency.

The light source was a 980 nm light-emitting diode (LED), with the fully-on intensity fixed at 1.1 mW cm^{-2} and the off-state in the dark. The rise/fall transition period t was varied from 0.01 to 7 ms, corresponding to $\Delta P/t$ inputs spanning 3 orders of magnitude from 110 to 0.170 W s^{-1} cm^{-2}. Faster rates of illumination change led to output spikes with sharper, higher peaks. Notably, the timing of the peak voltage V_{peak} differed between the rising and falling edges. The signal spikes were generated within 1 ms of switching the light on from the dark. In contrast, the spikes were spread out over time when switching the light off, emerging near the time when illumination dropped to zero, as charge displacement and recombination processes became more prominent at low light levels.

Figure 2c summarizes the peak magnitudes, showing that as transition rates $\Delta P/t$ increased, V_{peak} rose from 13 mV to 90 mV for the rising edge and from 6 mV to 32 mV for the falling edge. From these measurements and a sensor area of 0.01 cm^2, a lower limit of $\Delta P/t$ = 1 mW s^{-1} would generate a detectable spike. Assuming a rise/fall time of 0.01 ms, a light intensity change of ΔP = (1 mW s^{-1})(0.01 ms) = 0.01 μW would be the noise equivalent power for the photodetector here, which was comparable to prior retinomorphic sensors and better than photodiodes with similar organic infrared materials.[39,42] In Figure 2d, with faster transition rates, the spike full width at half-maximum (fwhm) was reduced from 670 to 100 μs for the rising

https://doi.org/10.1021/acsnano.6c00638
ACS Nano XXXX, XXX, XXX−XXX

edge and 750 to 200 μs for the falling edge. The V_{peak} magnitudes were normalized and plotted against the transition frequency (the inverse of the transition period, $1/t$), as shown in Figure 2e, exhibiting the characteristic behavior of a high-pass filter. The −3 dB cutoff frequencies for the rising and falling edges were 2 kHz and 1 kHz, respectively.

Vary Δ*P* While *t* Is Fixed. After assessing how transition time *t* affected spike output characteristics, we next investigated the effects of light intensity change ΔP, with particular attention paid to how the output was affected by background illumination P_B. In real-world environments, motion events occur against a backdrop of varying ambient light levels, not simple switching from light to complete darkness. To emulate realistic conditions, two light sources were used, with one LED modulated between light on/off at 100 Hz, and the second LED emitting a constant light level in the background, as illustrated in Figure 3a. A representative series of output characteristics is shown in Figure 3b, with the incident P_L at 1.1 mW cm^{-2} and the P_B varying from 0 to 1.2 μW cm^{-2}. As the background illumination increased, the effective intensity ΔP decreased, resulting in reduced V_{peak} magnitudes due to the diminishing input change.

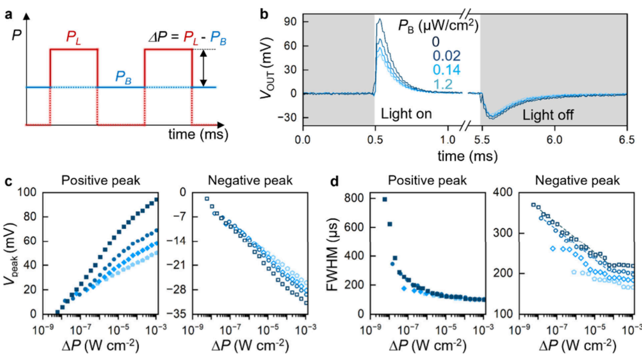

Figure 3. Photoresponse dynamics with background illumination. Measurements with a 100 kΩ resistor under two 980 nm LEDs. (a) Illustration of steady background illumination (blue) over light pulses (red). (b) Photoresponse to a light pulse of 1.1 mW/cm^2 under different background illumination levels from 0 to 1.2 μW/cm^2. Same color legend for parts b−d. (c) Output voltages and (d) full-width half-maximum of positive and negative peaks as a function of the intensity difference between light pulses and background illumination.

More intriguingly, after adjusting both P_L and P_B to reach the same ΔP in a set of measurements (data in supplemental Figure S4), a higher background P_B still led to lower V_{peak} magnitude, as seen in Figure 3c, where the dark blue data were taken under P_B = 0 W cm^{-2} and light blue data under P_B = 1.2 μW cm^{-2}. For ΔP below 0.1 μW cm^{-2}, the V_{peak} magnitudes were actually unaffected by the background light; the sensitivity curves of V_{peak} versus ΔP overlapped across different background conditions, indicating consistent signals even under elevated background. The sensitivity was 15 mV/decade, more sensitive than conventional organic photodiodes in open-circuit voltage mode.[43] However, for higher ΔP levels, the influence of background intensity became prominent; at ΔP = 0.1 mW cm^{-2}, V_{peak} dropped from 94 mV to 50 mV for the positive rising edge and from −32 mV to −26 mV for the negative falling edge.

The background illumination generated a reservoir of charge, reducing the ratio of displacement charge due to ΔP relative to the background charge from P_B. This phenomenon accounted for the V_{peak} decrease and was also consistent with the stronger background effect observed for the rising edge compared to the falling edge. For the falling edge, the negative peak magnitudes were smaller than their positive counterparts, and the signal originated from an existing charge reservoir (since light was already on). Thus, additional background charge had a limited effect, because the displacement and background charges were able to recombine through similar pathways to dissipate.

In contrast, for the rising edge, signal generation started from a less-occupied reservoir and was more sensitive to background charge level. If background charges accumulated, it would be more difficult for exciton dissociation and charge separation, leading to a reduction in the achievable peak magnitude. The linear dynamic range of the photodetector was 85 dB (for incident light intensity from 6 nW cm^{-2} to 0.11 mW cm^{-2}) when there was no background light and decreased to 58 dB (for incident light intensity from 1 μW cm^{-2} to 0.6 mW cm^{-2}) when the background level was at P_B = 1.2 μW cm^{-2}. On the other hand, the fwhm of output signals remained unchanged under background illumination for the positive peaks and became slightly narrower for the negative peaks in Figure 3d. The presence of additional background charge under illumination likely facilitated faster recombination during the falling edge, thereby reducing the fwhm. These sharper signal spikes under illuminated conditions would allow a higher refresh rate for

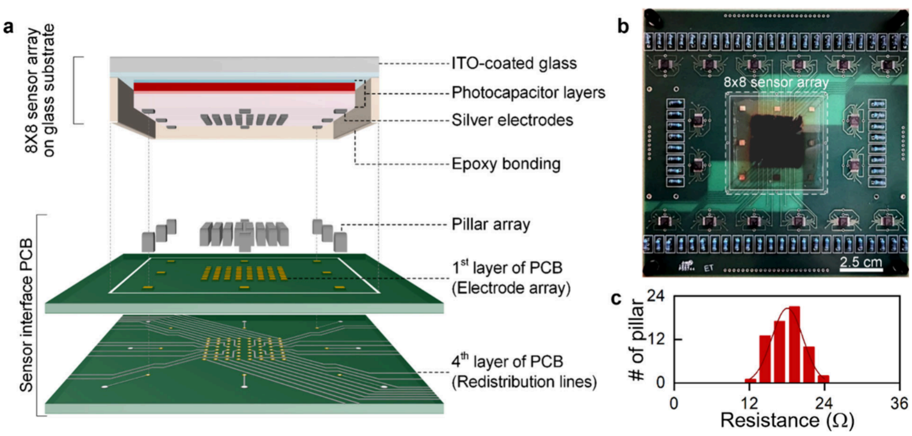

Figure 4. Design and fabrication of a retinomorphic infrared imager. (a) Integration schematics and (b) photograph of the 8 × 8 pixel array on a printed circuit board. Scale bar: 2.5 cm. (c) Resistance values of 64 pillar interconnects.

https://doi.org/10.1021/acsnano.6c00638
ACS Nano XXXX, XXX, XXX−XXX

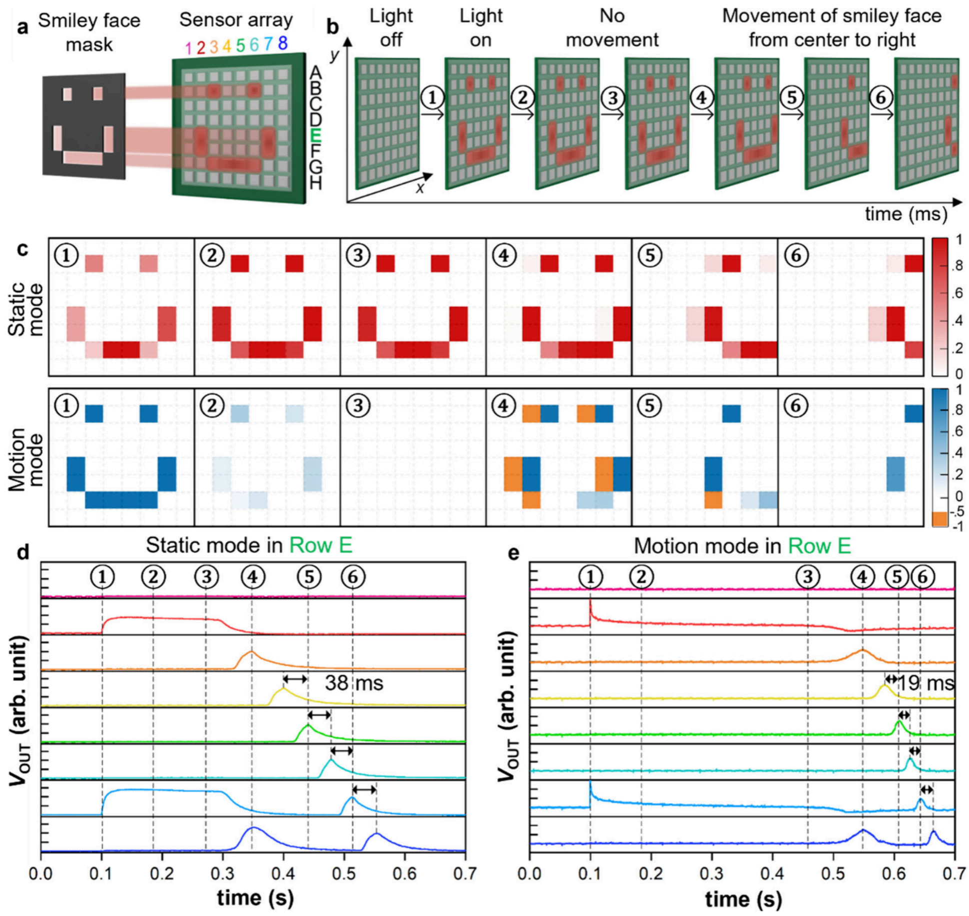

Figure 5. Imaging in static or motion mode. (a) Schematic of a light pattern projected through a mask onto the 8 × 8 pixel array. (b) Sequence of the projected pattern movement. (c) Spatiotemporal mapping of the array's response under static or motion-driven operating mode. In motion mode, positive voltage output is blue while negative voltage (below the threshold of −0.5) is orange. The color scale is normalized to the peak amplitude across the time series. Temporal response of the sensors at row E in (d) static or (e) motion mode. Data from the eight sensors in this row are displayed sequentially from the first sensor (top red) to the eighth (bottom blue). The circled numbers correspond to the time points in part b.

event detection. A comparison table of photosensor response speed is included in supplemental Table ST1.

Integration of Sensor Arrays with PCB

Electrically tunable sensors are appealing for their ease of control and have been demonstrated in organic photodetectors for spectral switching applications.[44−47] In this work, the concept of electrical tunability is extended to switch operation between high-fidelity frame-based imaging and streamlined event-driven motion tracking. To achieve spatial mapping, the photocapacitors are fabricated as an 8 × 8 pixel array and integrated onto a PCB interface with silicon IC chips. The photocapacitors were patterned on a glass substrate, and the entire array was aligned and bonded onto the PCB by applying epoxy at the substrate edges. The PCB pixel contact pads were modified with stencil-printed solder pillars serving as electrical interconnects, as shown in Figure 4a and supplemental Figure S5. For each retinomorphic sensor pixel, the photocapacitor was fabricated on the glass substrate, while the FET responsible for dual-mode control was in a discrete packaged Si chip on PCB. Thus, the PCB was a 4-layer board to route the 64 pixel pads to the periphery for IC connections, displayed in supplemental Figure S6. In the future, the photocapacitors can be directly bonded with FETs within active-matrix array architectures, but for now this proof-of-concept setup allows independent testing and validation of sensor arrays and various IC designs prior to full on-chip integration.

A photograph of the integrated imaging board is shown in Figure 4b, with the 8 × 8 photocapacitors in the center connected to switch ICs, resistors, voltage and signal nodes. Ensuring high-quality electrical connections between each sensor and its corresponding PCB pad was essential, since the interconnect resistance would contribute to the overall RC time constant, affecting the operating frequency and array uniformity. The resistance values of all 64 interconnects were measured in Figure 4c, with an average of 18.1 Ω and a standard deviation of 2.5 Ω. Given that the total resistive path in the dual-mode configuration was in either kΩ or 1 MΩ range, the interconnect resistance was negligible and well within acceptable limits.

Demonstration of Dual-Mode Imaging

For the dual-mode imaging array, mode selection was switched by toggling the FET gate voltage, and the signal was recorded using a data acquisition (DAQ) board with 8 input channels interfaced with 8 multiplexing circuits that managed sequential readout of rows A through H in Figure 5a. Supplemental Figure S7 shows the circuit diagram in detail, and supplemental Figure S8 presents the setup photograph and DAQ board connections. Variations across the array were evaluated by comparing the outputs of all 64 pixels under illumination from a 980 nm LED modulated at 200 Hz. The histograms of V_{peak} in supplemental Figure S9 quantified the relative standard deviation (RSD, defined as the standard deviation divided by the average). In the static mode, the RSD was 14%; in motion mode, it was 26% for the rising edge and 19% for the falling edge data. These low RSD values indicate successful integration and good uniformity across the array.

To provide an illustrative comparison of the dual imaging modes, we demonstrated an example in which a light pattern, created through a smiley-face mask, was scanned across the imager array, as depicted in Figure 5b. The temporal time points indicated the sequence of turning the light source on (1), holding the mask at the same location for some time (2, 3), and then moving the mask to the right side (4, 5, 6). The spatiotemporal data collected by the imager are plotted at those six time points in Figure 5c, while supplemental Movie SM1 presents the full data sequence.

When the light pattern was stationary between time points 1 to 3, the imager output stayed constant in static mode; but in motion mode, the signal began to dissipate by time point 2 and completely disappeared by time point 3 because of the retinomorphic discharging mechanism. When the mask was moved starting at time point 4, the image captured in static mode shifted to the right accordingly, with some blurring of the signal between pixels observed at time points 5 and 6. In the motion mode, the image was reconstructed from both positive and negative spikes. An increase in light level led to positive spikes denoted by blue color, while light decrease corresponded to negative spikes denoted by orange color. Due to movement at time point 4, both positive blue and negative orange signals were mapped in adjacent pixels, marking where light moved away from one pixel to its neighbor.

Another notable event-driven characteristic was observed in row G, columns 3−7, which were pixels lit up in static mode but not in motion mode. These pixels were exposed to constant light from the smile pattern and active in static mode; yet in motion mode, since there was no change in light level at those locations, the pixels were in equilibrium and not generating signal to minimize static redundancy. As the mask continued to move during time points 5 and 6, the advancing light front was indicated by the blue pixels shifting to the right. Negative spikes were not prominent, probably obscured within the fall time of the positive spikes. Nonetheless, the spiking signals in motion mode were much sharper than in static mode and significantly reduced motion blur artifacts.

A detailed view of pixel response simultaneously captured across pixels 1−8 in row E is presented in Figure 5d and Figure 5e under static and motion modes, respectively, and representative signals from rows B and G are also included in supplemental Figure S10. The exact time intervals between time points 1 to 6 differed across the data sets, because they were recorded in separate trials; but for each mode at least a dozen trials were conducted to confirm trend reproducibility. The movement of light from one pixel edge to the adjacent pixel edge was captured by the time difference between the signal peaks and determined to be 38 ms in static mode (Figure 5d) and 19 ms in motion mode (Figure 5e). With the pixel pitch of 2.54 mm, the mask movement speeds were calculated to be 66.8 and 133.6 mm/s in the two respective trials. The signal decay time in static mode was longer than 38 ms, resulting in motion blur, whereas in motion mode, the spike fwhm was less than the movement duration and enabled precise motion tracking.

■ CONCLUSIONS

This work presented a new approach for achieving the functionality of dual-mode imaging, where simple electrical biasing allows the sensor to operate in a conventional static mode for capturing detailed scene information or to work in a retinomorphic motion mode for in-sensor feature-extraction, delivering streamlined spiking data focused on motion tracking. The sensor design used a combination of a photocapacitor and a FET, as the voltage-adjustable channel resistance of the FET enabled mode selection. Due to the time-derivative nature of the design, we examined how the sensor outputs were affected by transition rate and background level change. These characterizations were essential for understanding detection limits in dynamic scenes under various background conditions. Once fully characterized, the sensors were integrated onto a PCB as a proof-of-concept 8 × 8 pixel array. The sensor-PCB integration enabled spatiotemporal imaging and showcased the complementary advantages of the two operation modes to reduce motion blur as needed or to capture high-fidelity images when desired. Looking forward, beyond scaling to larger arrays, the spiking behaviors of the photodetectors will be harnessed for on-chip signal processing, aiming toward next-generation neuromorphic imaging systems.

■ METHODS

Materials Preparation

For BHJ, the narrow bandgap polymer (poly(4-(5-(4-(3,5-bis-(dodecyloxy)-benzylidene)-4*H*-cyclopenta[2,1-*b*:3,4-*b*′]dithiophen-2-yl)thiophen-2-yl)-6,7-dioctyl-9-(thiophen-2-yl)-[1,2,5]thiadiazolo-[3,4-g]quinoxaline)) (CDT-TQ, synthesis procedure in ref 48) was blended with the fullerene derivative [6,6]-phenyl-C71-butyric acid methyl ester ($PC_{70}BM$) (>99%, Ossila Ltd.) at a weight ratio of 1:2 and dissolved in 1,2-dichlorobenzene (oDCB) (99%, Sigma-Aldrich) at a concentration of 30 mg mL^{-1}. To enhance charge dissociation and favorable morphology, camphoric acid anhydride and 1,8-diiodooctane were added to the blend solution at a volume ratio of 15% and 3%, respectively. This blended solution was stirred at 70 °C for 24 h in the glovebox. For high-κ dielectric, poly(vinylidene fluoride-trifluoroethylene-chlorotrifluoroethylene) terpolymer P(VDF-TrFE-CTFE) (RT-TS, Piezotech) was dissolved in *N*,*N*-dimethylformamide (DMF) (99%, Sigma-Aldrich) at a concentration of 150 mg mL^{-1}. The precursor solution of electron transporting layer SnO_2 was prepared by dissolving $SnCl_2$ in ethanol at a concentration of 0.07 M and then stirred in a water bath at 80 °C for 8 h.

Photocapacitor Fabrication

For the photocapacitor component of the retinomorphic sensor, an indium tin oxide (ITO, sheet resistance 15 Ω/sq) was coated on a 5 × 5 cm^2 glass substrate (Eagle XG, Corning). The precursor solution for the electron transport layer SnO_2 was spin-coated at 3000 rpm for 40 s and annealed at 180 °C for 1 h, to obtain a film thickness of 30 nm. The BHJ blend solution was spin-coated at 1000 rpm for 60 s on top of the SnO_2 layer to form a film with a thickness of 300 nm. For the hole transport layer, 10 nm thick molybdenum oxide (MoO_x) was deposited by thermal evaporation. The high-κ P(VDF-TrFE-CTFE) was spin-coated on top of the MoO_x layer at 3000 rpm for 90 s, resulting in a 300 nm thick film. A 100 nm Ag layer was thermally deposited through an 8 × 8 array mask, defining the pixel electrode area to be 0.01 cm^2.

PCB Design and Interconnect Pillar Array Fabrication

The PCB was designed in a four-layer configuration using PCB Artist Software (Advanced PCB). The top layer (1st) was consisted of the pads for 64 resistors, 64 sensors, and 16 switch IC packages each with 4 FETs (TMUX1511, Texas Instruments). The second and third layers (2nd and 3rd) served as internal power planes (V_{DD}, V_{in}, and ground nodes). The bottom layer (4th) routed signal redistribution lines. The sensor area was 1 × 1 mm^2 and the PCB size was 6 × 6 square inch. To

https://doi.org/10.1021/acsnano.6c00638
ACS Nano XXXX, XXX, XXX−XXX

pattern the pillar arrays, a stencil mask was patterned with openings of 1.1 × 1.1 mm^2 and placed to the PCB with the predefined printed electrode array. Solder paste (SP-30G-Sn42Bi58, Wonderway) and silver paint (PELCO Conductive Silver Paint 16062, Ted Pella) were mixed in a 7:3 volume ratio to increase conductivity and maintain the shape of the pillar. The mixture was deposited through the stencil mask. After printing, the stencil mask was removed, forming micrometer-tall pillar arrays on the PCB surface.

Photocapacitor-PCB Integration

The glass substrate carrying the photocapacitor array was prepared by cleaning the four edges to expose the bondable areas. An epoxy adhesive (Double Bubble Red 04001, Hardman) was then coated along the edges of the glass substrate. The glass substrate was flipped and aligned with the PCB prepared with pillar interconnects. The flip-bonding process was performed at room temperature and under hand pressure to ensure good contact between the sensor electrodes and the PCB pads. Finally, the epoxy was reflowed by gravity to ensure robust adhesion and mechanical stability of the integrated structure.

Device Characterization

The voltage outputs versus time were measured using an oscilloscope (DS1054z, Rigol) under ambient conditions. The light source was a LED with a peak wavelength of 980 nm (Thorlabs). The transition times for the rising and falling voltage input were controlled by a function generator (DG2041A, Rigol). To examine the impact of background illumination, the modulated LED (square waveform with rise/fall time of 10 μs for P_L) and the constantly-on LED (background input) were controlled by a function generator (DG2041A, Rigol) and a DC power supply (DPS3010U, Wanptek), respectively. The light intensity was calibrated using a germanium (Ge) detector (818-IR/DB, Newport). The retinomorphic sensors were operated under V_{in} = 0 V for all measurements and switched between static and motion modes using switch IC under V_{DS} = 1.8 V and V_{GS} = 0 V for gate off in static mode and V_{GS} = 1.8 V for gate on in motion mode.

Dual-Mode Imaging Demonstration

The response of the 8 × 8 pixel array was measured using eight channels of a DAQ board (USB-1608FS-Plus, Digilent) and was acquired using DAQami software (Measurement Computing). Each input channel was a 16-bit single-ended analog input and has a dedicated analog-to-digital converter for simultaneous sampling, in which voltage data in the ±1 V range were acquired at a rate of 50KS/s. The 8 sensors (#1−8) in a row were simultaneously monitored by the 8 DAQ input channels. To switch recording between rows (A−H) which enabled sequential access to all 64 pixels, the array readout was managed by using eight 8-to-1 multiplexers (MUXs) (CD74HC4051, Texas Instruments) connected with eight pull-down resistors of 1 MΩ. The four selectors of the MUXs were controlled by a field programmable gate array (FPGA) (ZYNQ-7000, Xilinx) to sequentially access the rows at 100 Hz intervals.

Equation for Frequency and Intensity Response

The normalized peak voltage ($V_{peak,norm}$) in decibel as a function of transition frequency is expressed as

$$V_{peak,norm} = 20 \log_{10}\left(\frac{V_{peak,f}}{V_0}\right)$$

where V_0 is the peak voltage measured at 50 Hz frequency. f is the measurement frequency.

The linear dynamic range (LDR) is defined by

$$\mathrm{LDR\ (dB)} = 10 \log_{10}\left(\frac{P_{max,lin}}{P_{min,lin}}\right)$$

where $P_{max,lin}$ and $P_{min,lin}$ denote the maximum and minimum light intensities within the linear photoresponse regime, respectively.

ASSOCIATED CONTENT

Supporting Information

The Supporting Information is available free of charge at https://pubs.acs.org/doi/10.1021/acsnano.6c00638.

- Supplemental figures content: Figure S1 showing materials and device structures and characterization; Figure S2 showing comparison of conventional photodiodes and dual-mode sensors; Figure S3 showing schematics of charge dynamics in the retinomorphic sensor; Figure S4 showing sensor response with background illumination; Figure S5 showing structure and fabrication process of the sensor array; Figure S6 showing PCB layout design and photograph; Figures S7 and S8 showing readout circuit schematics and photographs; Figure S9 showing pixel characterization; Figure S10 showing spatial and temporal response of the 8 × 8 array; Table ST1 showing comparison of response characteristics of various photodetectors (PDF)
- Movie SM1 showing full data sequence (MP4)

AUTHOR INFORMATION

Corresponding Authors

Mingu Kang − *Department of Electrical and Computer Engineering, University of California, San Diego, La Jolla, California 92023, United States*; Email: mingu@ucsd.edu

Tse Nga Ng − *Department of Electrical and Computer Engineering, University of California, San Diego, La Jolla, California 92023, United States*; orcid.org/0000-0001-6967-559X; Email: tnn046@ucsd.edu

Authors

Woojo Kim − *Department of Electrical and Computer Engineering, University of California, San Diego, La Jolla, California 92023, United States*; orcid.org/0000-0002-3517-0718

Zihan Xia − *Department of Electrical and Computer Engineering, University of California, San Diego, La Jolla, California 92023, United States*

Tianyu Zhao − *Department of Electrical and Computer Engineering, University of California, San Diego, La Jolla, California 92023, United States*

Sanyukta Datta Gupta − *School of Chemistry and Biochemistry and School of Materials Science and Engineering, Georgia Institute of Technology, Atlanta, Georgia 30332, United States*

Soong Ju Oh − *Department of Materials Science and Engineering, Korea University, Seoul 02841, Republic of Korea*; orcid.org/0000-0003-1434-8844

Jason D. Azoulay − *School of Chemistry and Biochemistry and School of Materials Science and Engineering, Georgia Institute of Technology, Atlanta, Georgia 30332, United States*; orcid.org/0000-0003-0138-5961

Complete contact information is available at: https://pubs.acs.org/10.1021/acsnano.6c00638

Author Contributions

W.K. performed the experimental design, device fabrication, measurements, and data analysis. S.D.G. and J.D.A. provided the organic infrared semiconductors. Z.X., T.Z., and S.J.O. assisted in the data analysis. M.K. and T.N.N. conceived and supervised the project. W.K. and T.N.N. wrote the manuscript. All authors contributed to the editing of the manuscript.

Notes

The authors declare no competing financial interest.

■ ACKNOWLEDGMENTS

This work was supported by the National Science Foundation (NSF) Award ECCS-2318990 for device development and Award DMR-2323665 for materials research. Part of the work was performed at the San Diego Nanotechnology Infrastructure of UCSD, which is supported by NSF ECCS-2025752. This work was partially supported by the National Research Foundation of Korea (NRF) grant funded by the Korea Government (MSIT) (RS-2024-00438059).

■ REFERENCES

(1) Liao, F.; Zhou, F.; Chai, Y. Neuromorphic Vision Sensors: Principle, Progress and Perspectives. *Journal of Semiconductors* **2021**, *42*, No. 013105.

(2) Kim, G.; Barangi, M.; Foo, Z.; Pinckney, N.; Bang, S.; Blaauw, D.; Sylvester, D. A 467nW CMOS Visual Motion Sensor with Temporal Averaging and Pixel Aggregation. In *2013 IEEE International Solid-State Circuits Conference Digest of Technical Papers*; IEEE, 2013; pp 480−481.

(3) Posch, C.; Serrano-Gotarredona, T.; Linares-Barranco, B.; Delbruck, T. Retinomorphic Event-Based Vision Sensors: Bioinspired Cameras with Spiking Output. *Proceedings of the IEEE* **2014**, *102* (10), 1470−1484.

(4) Chowdhury, S. S.; Sharma, D.; Kosta, A.; Roy, K. Neuromorphic Computing for Robotic Vision: Algorithms to Hardware Advances. *Communications Engineering* **2025**, *4* (1), 152.

(5) Choi, C.; Lee, G. J.; Chang, S.; Song, Y. M.; Kim, D. H. Inspiration from Visual Ecology for Advancing Multifunctional Robotic Vision Systems: Bio-Inspired Electronic Eyes and Neuromorphic Image Sensors. *Adv. Mater.* **2024**, *36* (48), No. 2412252.

(6) Mennel, L.; Symonowicz, J.; Wachter, S.; Polyushkin, D. K.; Molina-Mendoza, A. J.; Mueller, T. Ultrafast Machine Vision with 2D Material Neural Network Image Sensors. *Nature* **2020**, *579* (7797), 62−66.

(7) Zhang, Z.; Wang, S.; Liu, C.; Xie, R.; Hu, W.; Zhou, P. All-in-One Two-Dimensional Retinomorphic Hardware Device for Motion Detection and Recognition. *Nat. Nanotechnol* **2022**, *17* (1), 27−32.

(8) Lin, Q.; Li, C.; Xiong, H.; Zhang, M.; Qiao, J.; Wu, J.; Yang, L.; Wang, S.; Chen, H.; Wei, Y.; Zheng, D.; Lu, G.; Hao, X.; Yu, D.; Cai, Y.; Facchetti, A.; Huang, H. Event-Driven Retinomorphic Photodiode with Bio-Plausible Temporal Dynamics. *Nat. Nanotechnol* **2025**, *20*, 1213.

(9) Feng, G.; Zhang, X.; Tian, B.; Duan, C. Retinomorphic Hardware for In-Sensor Computing. *InfoMat* **2023**, *5* (9), No. e12473.

(10) Chen, J.; Zhou, Z.; Kim, B. J.; Zhou, Y.; Wang, Z.; Wan, T.; Yan, J.; Kang, J.; Ahn, J. H.; Chai, Y. Optoelectronic Graded Neurons for Bioinspired In-Sensor Motion Perception. *Nat. Nanotechnol* **2023**, *18* (8), 882−888.

(11) Long, T.; Zhou, H.; Ko, J.; Tan, H.; Lim, J.; Zhao, Y.; Kang, D.; Yoon, E.; Go, G. T.; Kim, S.; Lee, S. W.; Park, C. Y.; Choi, H.; Kim, H.; Yun, H. J.; Park, S. H.; Park, K. S.; Park, J. W.; Kim, M.; Cho, Y. S.; Jang, H. W.; Yang, W.; Park, M. H.; Bae, W. K.; van Dijken, S.; Bang, J.; Lee, T. W. Ferroelectric Quantum Dots for Retinomorphic In-Sensor Computing. *Adv. Mater.* **2025**, No. e04117.

(12) Choi, C.; Leem, J.; Kim, M. S.; Taqieddin, A.; Cho, C.; Cho, K. W.; Lee, G. J.; Seung, H.; Bae, H. J.; Song, Y. M.; Hyeon, T.; Aluru, N. R.; Nam, S. W.; Kim, D. H. Curved Neuromorphic Image Sensor Array Using a MoS2-Organic Heterostructure Inspired by the Human Visual Recognition System. *Nat. Commun.* **2020**, *11* (1), 5934.

(13) Wang, W.; Gao, S.; Wang, Y.; Li, Y.; Yue, W.; Niu, H.; Yin, F.; Guo, Y.; Shen, G. Advances in Emerging Photonic Memristive and Memristive-Like Devices. *Advanced Science* **2022**, *9* (28), No. 2105577.

(14) Xu, J.; Jiang, B.; Wang, W.; Guo, Z.; Gao, J.; Hu, X.; Qin, J.; Ran, L.; Lin, L.; Cai, S.; Li, Y.; Zhou, F. High-Order Dynamics in an Ultra-Adaptive Neuromorphic Vision Device. *Nat. Nanotechnol* **2025**, *20*, 1419.

(15) Wang, S.; Wang, C. Y.; Wang, P.; Wang, C.; Li, Z. A.; Pan, C.; Dai, Y.; Gao, A.; Liu, C.; Liu, J.; Yang, H.; Liu, X.; Cheng, B.; Chen, K.; Wang, Z.; Watanabe, K.; Taniguchi, T.; Liang, S. J.; Miao, F. Networking Retinomorphic Sensor with Memristive Crossbar for Brain-Inspired Visual Perception. *Natl. Sci. Rev.* **2021**, *8* (2), nwaa172.

(16) Wu, S. E.; Zeng, L.; Zhai, Y.; Shin, C.; Eedugurala, N.; Azoulay, J. D.; Ng, T. N. Retinomorphic Motion Detector Fabricated with Organic Infrared Semiconductors. *Advanced Science* **2023**, *10*, No. 2304688.

(17) Reissig, L.; Dalgleish, S.; Awaga, K. A Differential Photodetector: Detecting Light Modulations Using Transient Photocurrents. *AIP Adv.* **2016**, *6* (1), No. 015306.

(18) Trujillo Herrera, C.; Labram, J. G. A Perovskite Retinomorphic Sensor. *Appl. Phys. Lett.* **2020**, *117* (23), No. 233501.

(19) Trujillo Herrera, C.; Labram, J. G. An Organic Retinomorphic Sensor. *ACS Appl. Electron Mater.* **2022**, *4* (1), 92−98.

(20) Trujillo Herrera, C.; Labram, J. G. Quantifying the Performance of Perovskite Retinomorphic Sensors. *J. Phys. D Appl. Phys.* **2021**, *54* (47), No. 475110.

(21) Labram, J. G. Operating Principles of Zero-Bias Retinomorphic Sensors. *J. Phys. D Appl. Phys.* **2023**, *56* (6), No. 065105.

(22) Zhang, X.; Labram, J. G. Role of Blend Ratio in Bulk Heterojunction Organic Retinomorphic Sensors. *J. Mater. Chem. C Mater.* **2022**, *10* (36), 12998−13004.

(23) Long, Z.; Ding, Y.; Qiu, X.; Zhou, Y.; Kumar, S.; Fan, Z. A Dual-Mode Image Sensor Using an All-Inorganic Perovskite Nanowire Array for Standard and Neuromorphic Imaging. *Journal of Semiconductors* **2023**, *44* (9), No. 092604.

(24) Wang, F.; Hu, F.; Dai, M.; Zhu, S.; Sun, F.; Duan, R.; Wang, C.; Han, J.; Deng, W.; Chen, W.; Ye, M.; Han, S.; Qiang, B.; Jin, Y.; Chua, Y.; Chi, N.; Yu, S.; Nam, D.; Chae, S. H.; Liu, Z.; Wang, Q. J. A Two-Dimensional Mid-Infrared Optoelectronic Retina Enabling Simultaneous Perception and Encoding. *Nat. Commun.* **2023**, *14* (1), 1938.

(25) Guo, X.; Xie, M.; Addhya, A.; Linder, A.; Zvi, U.; Wang, S.; Yu, X.; Deshmukh, T. D.; Liu, Y.; Hammock, I. N.; Li, Z.; DeVault, C. T.; Butcher, A.; Esser-Kahn, A. P.; Awschalom, D. D.; Delegan, N.; Maurer, P. C.; Heremans, F. J.; High, A. A. Direct-Bonded Diamond Membranes for Heterogeneous Quantum and Electronic Technologies. *Nat. Commun.* **2024**, *15* (1), 8788.

(26) Ghosh, S.; Zheng, Y.; Zhang, Z.; Sun, Y.; Schranghamer, T. F.; Sakib, N. U.; Oberoi, A.; Chen, C.; Redwing, J. M.; Yang, Y.; Das, S. Monolithic and Heterogeneous Three-Dimensional Integration of Two-Dimensional Materials with High-Density Vias. *Nat. Electron* **2024**, *7* (10), 892−903.

(27) Kim, W.; Ryu, G.; Nam, Y.; Choi, H.; Wang, M.; Kwon, J.; Nielsen, C. B.; Kang, K.; Jung, S. High Mobility Amorphous Polymer-Based 3D Stacked Pseudo Logic Circuits through Precision Printing. *Adv. Funct Mater.* **2024**, *34* (32), No. 2312922.

(28) Kim, W.; Jung, S. Static Response of Three-Dimensional and Printed Complementary Organic TFTs-Based Static Random-Access Memory. *IEEE Electron Device Lett.* **2022**, *43* (3), 438−441.

(29) Choi, C.; Kim, H.; Kang, J. H.; Song, M. K.; Yeon, H.; Chang, C. S.; Suh, J. M.; Shin, J.; Lu, K.; Park, B. I.; Kim, Y.; Lee, H. E.; Lee, D.; Lee, J.; Jang, I.; Pang, S.; Ryu, K.; Bae, S. H.; Nie, Y.; Kum, H. S.; Park, M. C.; Lee, S.; Kim, H. J.; Wu, H.; Lin, P.; Kim, J. Reconfigurable Heterogeneous Integration Using Stackable Chips with Embedded Artificial Intelligence. *Nat. Electron* **2022**, *5* (6), 386−393.

(30) Ready, S.; Endicott, F.; Whiting, G.; Ng, T. N.; Chow, E.; Lu, J.-P. 3D Printed Electronics. *NIP & Digital Fabrication Conference* **2013**, *29* (1), 9−12.

(31) Kim, W.; Kim, S. K.; Jeon, S.; Ahn, J.; Jung, B. K.; Lee, S. Y.; Shin, C.; Seong, T. Y.; Jeong, S.; Jang, H. S.; Ng, T. N.; Oh, S. J. Patterning All-Inorganic Halide Perovskite with Adjustable Phase for High-Resolution Color Filter and Photodetector Arrays. *Adv. Funct Mater.* **2022**, *32* (16), No. 2111409.

(32) Yao, L.; Koripally, N.; Shin, C.; Mu, A.; Chen, Z.; Wang, K.; Ng, T. N. Engineering Electro-Crystallization Orientation and Surface Activation in Wide-Temperature Zinc Ion Supercapacitors. *Nat. Commun.* **2025**, *16* (1), 3597.

(33) Ng, T. N.; Schwartz, D. E.; Mei, P.; Krusor, B.; Kor, S.; Veres, J.; Bröms, P.; Eriksson, T.; Wang, Y.; Hagel, O.; Karlsson, C. Printed Dose-Recording Tag Based on Organic Complementary Circuits and Ferroelectric Nonvolatile Memories. *Sci. Rep.* **2015**, *5*, No. 13457.

(34) Bills, T.; Liu, C. T.; Lim, J.; Eedugurala, N.; Mahalingavelar, P.; Seo, B.; Hanna, E. T.; Ng, T. N.; Azoulay, J. D. A General Strategy for Enhancing Sensitivity and Suppressing Noise in Infrared Organic Photodetectors Using Non-Conjugated Polymer Additives. *Adv. Funct Mater.* **2024**, *34* (24), No. 2314210.

(35) Park, I.; Kim, C.; Kim, R.; Li, N.; Lee, J.; Kwon, O. K.; Choi, B.; Ng, T. N.; Leem, D.-S. High Performance Shortwave Infrared Organic Photodetectors Adopting Thiadiazole Quinoxaline-Based Copolymers. *Adv. Opt Mater.* **2022**, *10* (19), No. 2200747.

(36) Huang, J.; Lee, J.; Vollbrecht, J.; Brus, V. V.; Dixon, A. L.; Cao, D. X.; Zhu, Z.; Du, Z.; Wang, H.; Cho, K.; Bazan, G. C.; Nguyen, T. Q. A High-Performance Solution-Processed Organic Photodetector for Near-Infrared Sensing. *Adv. Mater.* **2020**, *32* (1), No. 1906027.

(37) Li, N.; Park, I.; Vella, J. H.; Oh, S. J.; Azoulay, J. D.; Leem, D.-S.; Ng, T. N. Contribution of Sub-Gap States to Broadband Infrared Response in Organic Bulk Heterojunctions. *ACS Appl. Mater. Interfaces* **2022**, *14* (47), 53111−53119.

(38) Sulas, D. B.; London, A. E.; Huang, L.; Xu, L.; Wu, Z.; Ng, T. N.; Wong, B. M.; Schlenker, C. W.; Azoulay, J. D.; Sfeir, M. Y. Preferential Charge Generation at Aggregate Sites in Narrow Band Gap Infrared Photoresponsive Polymer Semiconductors. *Adv. Opt Mater.* **2018**, *6*, No. 1701138.

(39) Shin, C.; Li, N.; Seo, B.; Eedugurala, N.; Azoulay, J. D.; Ng, T. N. Heterojunction Bilayers Serving as a Charge Transporting Interlayer Reduce the Dark Current and Enhance Photomultiplication in Organic Shortwave Infrared Photodetectors. *Mater. Horiz* **2022**, *9* (8), 2172−2179.

(40) Li, N.; Lim, J.; Azoulay, J. D.; Ng, T. N. Tuning the Charge Blocking Layer to Enhance Photomultiplication in Organic Shortwave Infrared Photodetectors. *J. Mater. Chem. C Mater.* **2020**, *8*, 15142−15149.

(41) Pecunia, V.; Anthopoulos, T. D.; Armin, A.; Bouthinon, B.; Caironi, M.; Castellanos-Gomez, A.; Chen, Y.; Cho, K.; Clegg, C.; Fang, X.; Fendel, P.; Fowler, B.; Gelinck, G.; Gottlob, H.; Guyot-Sionnest, P.; Hannebauer, R.; Hernandez-Sosa, G.; Hersam, M. C.; Hirsch, L.; Ho, J. C.; Isikgor, F. H.; Joimel, J.; Kim, H. J.; Konstantatos, G.; Labram, J.; Lemme, M. C.; Leo, K.; Lhuillier, E.; Lidorikis, E.; Loi, M. A.; Malinowski, P. E.; Merken, P.; Mueller, T.; Nasrollahi, B.; Natali, D.; Ng, T. N.; Nguyen, T.-Q.; Park, S. K.; Peng, L.-M.; Samorì, P.; Sargent, E. H.; Shen, L.; Shishido, S.; Shorubalko, I.; Sonar, P.; Stranks, S. D.; Tedde, S. F.; Vandewal, K.; Verhaegen, M.; Walia, S.; Yan, F.; Yokota, T.; Zhang, F. Guidelines for Accurate Evaluation of Photodetectors Based on Emerging Semiconductor Technologies. *Nat. Photonics* **2025**, *19* (11), 1178−1188.

(42) Seo, B.; Chung, J.; Eedugurala, N.; Azoulay, J. D.; Kim, H. J.; Ng, T. N. Bias Dependence of Organic-Oxide Phototransistors with Peak Infrared Absorption at 1550 Nm. *ACS Appl. Electron Mater.* **2023**, *5* (11), 6401−6407.

(43) Kielar, M.; Hamid, T.; Wiemer, M.; Windels, F.; Hirsch, L.; Sah, P.; Pandey, A. K. Light Detection in Open-Circuit Voltage Mode of Organic Photodetectors. *Adv. Funct Mater.* **2020**, *30* (9), No. 1907964.

(44) Lan, Z.; Zhu, F. Electrically Switchable Color-Selective Organic Photodetectors for Full-Color Imaging. *ACS Nano* **2021**, *15*, No. 13674.

(45) Lan, Z.; Lei, Y.; Chan, W. K. E.; Chen, S.; Luo, D.; Zhu, F. Near-Infrared and Visible Light Dual-Mode Organic Photodetectors. *Sci. Adv.* **2020**, *6* (5), No. eaaw8065.

(46) Li, N.; Eedugurala, N.; Azoulay, J. D.; Ng, T. N. A Filterless Organic Photodetector Electrically Switchable between Visible and Infrared Detection. *Cell Rep. Phys. Sci.* **2022**, *3* (1), No. 100711.

(47) He, X.; Li, Y.; Yu, H.; Zhou, G.; Ke, L.; Yip, H. L.; Zhao, N. A Microsized Optical Spectrometer Based on an Organic Photodetector with an Electrically Tunable Spectral Response. *Nat. Electron* **2024**, *7* (8), 694−704.

(48) Wu, Z.; Zhai, Y.; Yao, W.; Eedugurala, N.; Zhang, S.; Huang, L.; Gu, X.; Azoulay, J. D.; Ng, T. N. The Role of Dielectric Screening in Organic Shortwave Infrared Photodiodes for Spectroscopic Image Sensing. *Adv. Funct Mater.* **2018**, *28* (50), No. 1805738.

https://doi.org/10.1021/acsnano.6c00638
ACS Nano XXXX, XXX, XXX−XXX